J. Fluid Mech. (2008), *vol.* 605, *pp.* 329–354.
doi:10.1017/S0022112008001468 Printed in the United Kingdom

Numerical simulation of the fluid dynamic effects of laser energy deposition in air

SHANKAR GHOSH AND KRISHNAN MAHESH

Aerospace Engineering and Mechanics, University of Minnesota, MN 55455, USA

(Received 8 June 2006 and in revised form 6 March 2008)

Numerical simulations of laser energy deposition in air are conducted. Local thermodynamic equilibrium conditions are assumed to apply. Variation of the thermodynamic and transport properties with temperature and pressure are accounted for. The flow field is classified into three phases: shock formation; shock propagation; and subsequent collapse of the plasma core. Each phase is studied in detail. Vorticity generation in the flow is described for short and long times. At short times, vorticity is found to be generated by baroclinic means. At longer times, a reverse flow is found to be generated along the plasma axis resulting in the rolling up of the flow field near the plasma core and enhancement of the vorticity field. Scaling analysis is performed for different amounts of laser energy deposited and different Reynolds numbers of the flow. Simulations are conducted using three different models for air based on different levels of physical complexity. The impact of these models on the evolution of the flow field is discussed.

1. Introduction

The deposition of laser energy into air has been studied by a number of workers (e.g. Damon & Tomlinson 1963; Knight 2003; Maker, Terhune & Savage 1963; Meyerand & Haught 1963; Root 1989), and finds application in localized flow control of supersonic flows (Adelgren *et al.* 2003; Shneider *et al.* 2003), drag reduction in supersonic and hypersonic flows (Riggins, Nelson & Johnson 1999), ignition of combustion gases (Phuoc 2000) and provision of thrust to aerospace vehicles (Molina-Morales *et al.* 2001; Wang *et al.* 2001). When a laser beam is focused on a small volume of gas, the gas molecules in the focal volume absorb energy and are ionized. A simple description of the plasma formation process is as follows (Raizer 1966; Morgan 1975; Keefer 1989; Phuoc 2005). Electrons are initially released owing to multi-photon ionization, when multiple photons are simultaneously incident on an atom. During this process, the electron number density increases linearly in time. The released electrons absorb laser energy owing to inverse bremsstrahlung absorption, where a free electron in the presence of a third body absorbs energy and becomes excited. After many such interactions, the electron gains sufficient energy to impact-ionize neutral atoms. The electron concentration then increases exponentially in time. The resulting plasma reflects part of the incident laser energy. This energy is absorbed by adjacent molecules along the laser axis in the direction of the laser source. These molecules then become ionized, and start reflecting laser radiation. This process continues until the plasma evolves into a tear-drop shape. The collision of energetic electrons with heavy particles results in heating of the gas. Also, the electron number density decreases owing to recombination of the electrons with ions. A region where

temperature and pressure are higher than that of the surroundings is obtained at the end of plasma formation. The resulting pressure gradients lead to formation of a blast wave that propagates into the background gas.

Recent experiments on pulsed laser-induced breakdown include Jiang *et al.* (1998), Lewis *et al.* (1999), Adelgren, Boguszko & Elliott (2001) and Glumac, Elliott & Boguszko (2005*a,b*). Jiang *et al.* (1998) focused a laser beam of 1.38 J on a 3 mm diameter spherical region to cause breakdown of air. The laser was pulsed for a duration of 18 ns. Adelgren *et al.* (2001) pulsed a Nd:YAG laser of 200 mJ for 10 ns in air. The experimental data show a wide separation in time scales between laser pulse duration and blast wave propagation, i.e. the laser is pulsed on a time scale of 10 ns while the blast wave is observed on a time scale of 10 to 100 μs. Since the plasma forms on the time scale of the laser pulse duration, there is a three to four order of magnitude separation in time scale. The plasma may therefore be assumed to form instantaneously, to evaluate its gas-dynamic effect on the surrounding fluid.

Various simulation models have been used to understand different features of this phenomenon. Brode (1955) numerically simulated the blast wave and concluded that the ideal gas assumption was reasonable for shock pressures of less than 10 atm in air. Steiner, Gretlef & Hirschler (1998) perform computations using a real-gas model to show that when initialized with a self-similar strong-shock solution, the shock radius in the real-gas model is quite close to that predicted by the classical point-source explosion in an ideal gas. Other computations of blast-wave propagation in quiescent air include those by Jiang *et al.* (1998) and Yan *et al.* (2003). Dors, Parigger & Lewis (2000) and Dors & Parigger (2003) present a computational model which considers the asymmetry of laser energy deposition as well as ionization and dissociation effects on fluid properties. The initial stages of plasma formation due to laser energy deposition were modelled by Kandala & Candler (2003) and Kandala *et al.* (2005). Very few simulations account for the physical tear-drop shape of the plasma. Even simulations with complex physical models do not show the prominent flow features observed in experiment. One of the objectives of this paper is to investigate the level of physical complexity required to simulate accurately the flow features observed in the experiments. This paper considers generation of laser-induced plasma in quiescent air. Local thermodynamic equilibrium conditions are assumed to apply. The simulations are conducted using three different models for air based on different levels of physical complexity. Figure 1 shows a schematic of the problem. The relevant parameters associated with the problem are the shape and size of the initial plasma region, the maximum temperature ratio in the plasma core T_0 and viscosity of the fluid. The time evolution of the resulting flow field is divided into shock formation, shock propagation and subsequent roll-up of the plasma core. Each stage is discussed in detail. An explanation of the process of the rolling up of the plasma core is provided. Vorticity is found to be generated at short and long times through different mechanisms. At short times, vorticity generated in the flow is due to baroclinic production whereas at long times, vorticity is generated owing to rolling up of the plasma core. These mechanisms are studied in detail. Scaling analysis is performed for different values of T_0 and the Reynolds number of the flow. A Fourier spectral solver is developed for conducting the simulations. Numerical challenges associated with the simulations are discussed in detail.

This paper is organized as follows. Section 2 discusses the primary numerical challenges posed by the flow, and describes the numerical methodology. Simulation results are discussed in § 3. Section 3.1 starts with an overview of the flow field and then proceeds to describe the flow in each of the three phases of shock formation,

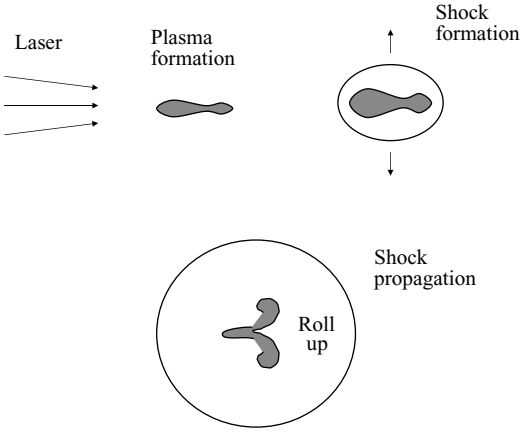

FIGURE 1. Schematic showing stages involved in laser-induced breakdown of a gas.

propagation and collapse of the core. The evolution of velocity, temperature and vorticity are discussed. The effect of maximum initial core temperature T_0 and Reynolds number on the flow is discussed in § 3.2. Section 3.3 shows simulation results from three different models used for air. A short summary in § 4 concludes the paper.

2. Simulation methodology

2.1. *Governing equations*

The Navier–Stokes equations are used to simulate the flow field resulting from the deposition of laser energy in air. Local thermodynamic equilibrium conditions are assumed to apply. Also, radiation losses after formation of the plasma spot are assumed to be negligible. Hence, the governing equations do not have additional source terms. The continuity, and compressible Navier–Stokes equations are given by

$$\frac{\partial \rho}{\partial t} + \frac{\partial \rho u_i}{\partial x_i} = 0, \tag{2.1}$$

$$\frac{\partial \rho u_j}{\partial t} + \frac{\partial \rho u_j u_i}{\partial x_i} = -\frac{\partial}{\partial x_i}\left[p\delta_{ij} - \frac{\mu}{Re}\left(\frac{\partial u_i}{\partial x_j} + \frac{\partial u_j}{\partial x_i} - \frac{2}{3}\frac{\partial u_k}{\partial x_k}\delta_{ij}\right)\right], \tag{2.2}$$

$$\frac{\partial \rho e_T}{\partial t} + \frac{\partial \rho e_T u_i}{\partial x_i} = \frac{\partial}{\partial x_i}\left[-pu_i + \frac{\mu}{Re}\left(\frac{\partial u_i}{\partial x_j} + \frac{\partial u_j}{\partial x_i} - \frac{2}{3}\frac{\partial u_k}{\partial x_k}\delta_{ij}\right)u_j\right] + \frac{\partial}{\partial x_i}\left(\frac{\kappa}{(\gamma-1)RePr}\frac{\partial T}{\partial x_i}\right) \tag{2.3}$$

where all the variables are non-dimensionalized by their initial background values.

$$\left.\begin{array}{c} x_i = x_i^*/L_0^*, \quad u_i = u_i^*/c_0^*, \quad t = t^* c_0^*/L_0^*, \\ \rho = \rho^*/\rho_0^*, \quad p = p^*/\rho_0^* c_0^{*2}, \quad T = T^*/T_0^* \\ \mu = \mu^*/\mu_0^*, \quad \kappa = \kappa^*/\kappa_0^*. \end{array}\right\} \tag{2.4}$$

Here, the subscript '0' denotes initial background values and the superscript, asterisk denotes dimensional variables. L_0^* is the reference length scale and is obtained by comparing the non-dimensional length of the plasma region used in the simulations

to the physical length of the plasma. c_0^* is the speed of sound based on initial background temperature; i.e.

$$c_0^* = (\gamma R^* T_0^*)^{1/2}. \tag{2.5}$$

The Reynolds number and Prandtl number are defined as

$$Re = \rho_0^* c_0^* L_0^* / \mu_0^*, \quad Pr = \mu^* c_p^* / k^*. \tag{2.6}$$

Simulations are conducted using models with three different levels of physical complexity. These models are described below.

2.1.1. *Model* 1

For the simplest case (model 1), the effects of chemical reactions resulting from high temperatures in the flow are neglected. Ideal-gas relations are used to represent the thermodynamic properties of air. Simple constitutive relations are assumed for the transport properties. The coefficient of viscosity is described by the power law

$$\mu = T^{0.67}, \tag{2.7}$$

the coefficient of thermal conductivity is obtained by assuming a constant Prandtl number of 0.7, and γ is assumed to be 1.4. The non-dimensionalized equation of state becomes

$$p = \rho T / \gamma, \tag{2.8}$$

where the temperature is related to the internal energy by the relation

$$T = \gamma(\gamma - 1)e, \tag{2.9}$$

and the total energy is related to internal energy and kinetic energy as

$$\rho e_T = \rho e + \tfrac{1}{2}\rho u_i u_i. \tag{2.10}$$

To obtain the initial conditions, a three-dimensional temperature profile is used to represent the heating effect of laser energy deposition. Since the energy addition is on a very fast time scale, the density is assumed constant. The initial pressure profile is then obtained using (2.15) and the internal energy e is obtained using (2.9). At the end of every time step, pressure and temperature are obtained from the conserved variables using the above constitutive equations.

2.1.2. *Model* 2

Model 2 considers the effect of chemical reactions resulting in dissociation, ionization and recombination of different species. Thermodynamic and transport properties for air are computed up to a temperature of 30 000 K. An 11 species model for air is considered; the species are

$$N_2,\ O_2,\ NO,\ N,\ O,\ N_2^+,\ O_2^+,\ NO^+,\ N^+,\ O^+ \text{ and } e^-,$$

and the compositions of individual species are obtained using the law of mass action. Then the mixture properties are obtained as a function of temperature based on the composition of the individual species. These properties are validated against data from the NASA code *CEA* (McBride & Gordon 1961, 1967, 1976, 1992; McBride *et al.* 1963). Also, the properties are computed for different values of pressure ranging from 1 to 300 atm. Model 2 uses only data computed for a pressure of 1 atm, i.e. it ignores the variation of these properties with pressure.

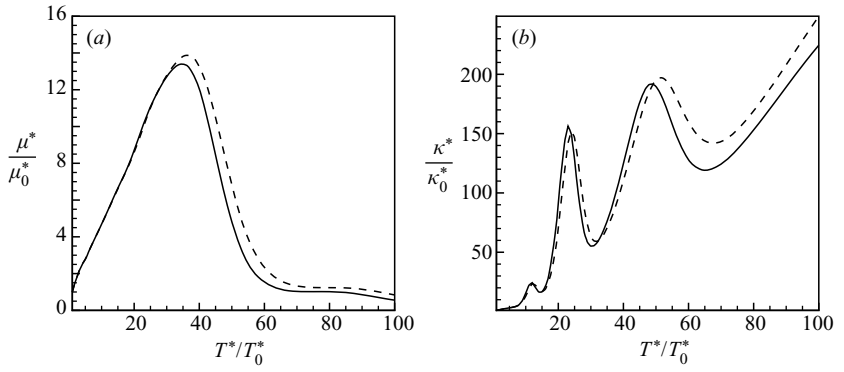

FIGURE 2. (*a*) Variation of the coefficient of viscosity μ with temperature T and pressure p. (*b*) Variation of the coefficient of thermal conductivity κ with temperature T and pressure p. ——, $p = 1\,\text{atm}$; – – –, $p = 10\,\text{atm}$.

The speed of sound based on initial background temperature is given by

$$c_0^* = (\gamma_0 R_0^* T_0^*)^{1/2}. \tag{2.11}$$

The dimensional coefficients of viscosity and thermal conductivity $\mu(T)^*$ and $\kappa(T)^*$ are shown in figure 2. The equation of state in non-dimensional form is now written as

$$p = \rho R(T) T, \tag{2.12}$$

where

$$R(T) = R^*(T)/\gamma_0 R_0, \tag{2.13}$$

and the variation of R^* with temperature is shown in figure 3(*c*). The total energy is related to internal energy and kinetic energy through (2.10) and temperature is obtained from internal energy using the equilibrium dependence of internal energy on temperature shown in figure 3(*a*). The Reynolds number and Prandtl number are given by

$$Re = \rho_0^* c_0^* L_0^*/\mu_0^*, \quad Pr = \mu_0^* c_{p0}^*/\kappa_0^*. \tag{2.14}$$

The initial pressure profile is obtained using $\rho = \rho_0$ in (2.12) and data for variation of R with temperature. The internal energy e is then obtained from the value of temperature (figure 3*a*) using cubic spline interpolation. The total energy is related to internal energy and kinetic energy through (2.10). At the end of every time step, temperature is obtained from values of e using data shown in figure 3(*a*). Once the temperature field is known, the pressure field is obtained as before.

2.1.3. *Model* 3

Model 3 takes into account the effects of pressure variation on the properties. Pressures in the flow are quite high at initial times and so the pressure variation of the thermodynamic properties can affect the flow. In particular, the effect on the initial conditions could be significant. The equation of state is given by

$$p = \rho R(T, p) T, \tag{2.15}$$

where

$$R(T, p) = R^*(T, p)/(\gamma_0 R_0^*), \tag{2.16}$$

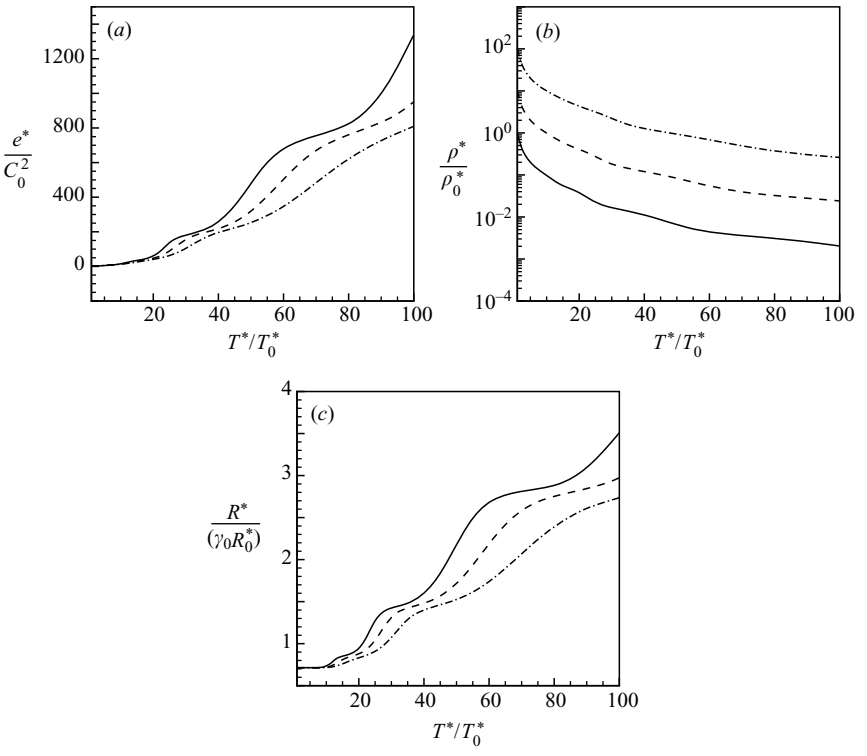

FIGURE 3. (*a*) Variation of internal energy e with temperature T and pressure p. (*b*) Variation of density ρ with temperature T and pressure p. (*c*) Variation of R with temperature T and pressure p. ——, $p = 1\,\text{atm}$; – – –, $p = 10$ atm; —·—, $p = 100\,\text{atm}$.

and the variation of R with temperature and pressure is shown in figure 3(*c*). The initial pressure is obtained through a process of iteration using $\rho = \rho_0$ in (2.15) and data for variation of R with pressure and temperature. The internal energy e is then obtained from the values of pressure and temperature (figure 3*a*). The total energy is related to internal energy and kinetic energy through (2.10). At the end of every time step, pressure and temperature are obtained from the values of ρ and e using the equilibrium data for $e(T, p)$ and $\rho(T, p)$ shown in figure 3.

2.2. *Fourier discretization*

The Navier–Stokes equations are solved using Fourier methods to compute the spatial derivatives. Any variable f is discretely represented as

$$f(x_1, x_2, x_3) = \sum_{k_1=-N_1/2}^{N_1/2-1} \sum_{k_2=-N_2/2}^{N_2/2-1} \sum_{k_3=-N_3/2}^{N_3/2-1} \hat{f}(k_1, k_2, k_3) \mathrm{e}^{(k_1 x_1 + k_2 x_2 + k_3 x_3)}, \tag{2.17}$$

where $\hat{f}(k_1, k_2, k_3)$ are the Fourier coefficients of f, and N_1, N_2 and N_3 are the number of points used to discretize the domain along x_1, x_2 and x_3, respectively. The Fourier coefficients of the spatial derivatives are therefore

$$\widehat{\frac{\partial f}{\partial x_\alpha}} = \mathrm{i} k_\alpha \widehat{f}, \quad \widehat{\frac{\partial^2 f}{\partial x_\alpha x_\alpha}} = -k_\alpha^2 \hat{f}. \tag{2.18}$$

A collocated approach is used, and the solution is advanced in time using a fourth-order Runge–Kutta scheme. The skew-symmetric form of the convection terms

$$\frac{\partial fg}{\partial x_j} = \frac{1}{2}\left[\frac{\partial fg}{\partial x_j} + f\frac{\partial g}{\partial x_j} + g\frac{\partial f}{\partial x_j}\right], \tag{2.19}$$

is used to suppress aliasing errors resulting from the nonlinear convection terms (Blaisdell, Mansour & Reynolds 1991). The above algorithm is implemented for parallel platforms using MPI. The library FFTW is used to compute Fourier transforms, and a pencil data structure is used. Each processor stores data along the entire extent of the x_1-direction, while data along the x_2- and x_3-directions are equally distributed among the processors. Fourier transforms along the x_1-direction are therefore readily computed, whereas transforms in the other directions require that the data be transposed prior to transforming.

The solver assumes periodic boundary conditions in each of the x_1-, x_2- and x_3-directions. The flow field resulting from laser energy deposition is axisymmetric and non-stationary in time. The periodic boundary conditions are valid as long as the blast wave does not reach the domain boundaries. This is because if the blast wave is well resolved, the gradients ahead of it will be zero.

2.3. *Shock capturing*

Recall that a strong shock wave propagates through the flow domain, when energy is added instantaneously. Experiments in laser-induced breakdown (e.g. Yan *et al.* 2003) show that the maximum temperature in the core is very high. This leads to sharp gradients in the flow variables. Since the flow solver uses spectral methods for spatial discretization, resolving these sharp gradients requires a highly refined mesh. The computational cost therefore increases significantly with increasing core temperatures. The Fourier spectral method is therefore combined with a shock-capturing scheme proposed by Yee, Sandham & Djomehri (1999), to avoid resolving the shock thickness.

The shock-capturing scheme is based on the finite-volume methodology, and is applied as a corrector step to the Fourier discretization used in this paper. In the first step, the predicted form of the solution vector is obtained using Fourier methods as discussed in § 2.2. This solution vector is then corrected using the numerical fluxes obtained from a characteristic based filter

$$U^{n+1} = \widehat{U}^{n+1} + \Delta t\left[\frac{1}{\Delta x}\left(\widetilde{F}^{\star}_{i+1/2,j,k} - \widetilde{F}^{\star}_{i-1/2,j,k}\right) + \frac{1}{\Delta y}\left(\widetilde{G}^{\star}_{i,j+1/2,k} - \widetilde{G}^{\star}_{i,j-1/2,k}\right) + \frac{1}{\Delta z}\left(\widetilde{H}^{\star}_{i,j,k+1/2} - \widetilde{H}^{\star}_{i,j,k-1/2}\right)\right]. \tag{2.20}$$

The filter numerical flux vector is of the form

$$\widetilde{F}^{\star}_{i+1/2,j,k} = \tfrac{1}{2}R_{i+1/2,j,k}\phi^{\star}_{i+1/2,j,k}, \tag{2.21}$$

where R is the right eigen vector matrix. The elements of $\phi^{\star}$ are denoted by $\phi^{l\star}$ and are given by

$$\phi^{l\star}_{i+1/2,j,k} = \kappa\theta^{l}_{i+1/2,j,k}\phi^{l}_{i+1/2,j,k}. \tag{2.22}$$

The parameter κ is problem dependent and lies between 0.03 and 2 (Yee *et al.* 1999). $\kappa = 1.0$ is used in all simulations reported in this paper. The function $\theta^{l}_{i+1/2,j,k}$ is the Harten switch (Harten 1978) and depends on the left eigen vector matrix L. The

formulation used for $\phi^l_{i+1/2,j,k}$ is given by the Harten–Yee upwind TVD form (Yee *et al.* 1999).

The Yee *et al.* approach was extended to the high-temperature equations in order to remain consistent with the predictor step. Computation of the eigen vector matrices R and L were suitably modified. The specific heats at constant pressure and volume C_P and C_V are no longer constants, but depend strongly on temperature and pressure. All other thermodynamic and transport properties are also functions of temperature and pressure. Thus to compute the eigen vector matrices, the Jacobian matrix $\partial \boldsymbol{F}/\partial \boldsymbol{U}$ must be recomputed. Here $\boldsymbol{F}$ denotes the flux vector and $\boldsymbol{U}$ denotes the vector of the conserved variables. Suitable forms of the Jacobian matrix were obtained for all three models described in § 2.1. These Jacobian matrices are given in the Appendix.

2.4. *Logarithm formulation of the continuity equation*

When laser energy is added to a flow at rest, there is noticeable expansion of the core. This results in very small values of the density in the core. When the continuity equation was advanced in time with density as the dependent variable, the solution was found to become unstable. It was therefore decided to solve for the logarithm of density as the variable. Define

$$v = \ln \rho \quad \Rightarrow \quad \rho = \mathrm{e}^v. \tag{2.23}$$

The continuity equation becomes

$$\frac{\partial v}{\partial t} + u_i \frac{\partial v}{\partial x_i} = -\frac{\partial u_i}{\partial x_i}, \tag{2.24}$$

Note that ρ is always positive when computed as e^v, even for very small values of ρ. The $\log \rho$ formulation of the continuity equation therefore makes the solution stable in regions of very low density.

3. Simulation results

Experiments in laser-induced breakdown (Adelgren *et al.* 2001; Yan *et al.* 2003) show that the plasma is initially tear-drop shaped. The simulations reported in this section are three-dimensional and the laser axis is located along the x_1-direction at the centre of the domain. Energy deposition is symmetric about the laser axis. Figure 4(*a*) shows the axial temperature distribution that is used to model the initial temperature profile of the plasma. This temperature distribution is obtained from simulations of Kandala (2005) who models the initial plasma formation in detail. The temperature profile normal to the plasma axis is assumed to be a Gaussian. The ratio of the maximum temperature in the plasma core to the background temperature, T_0, determines the amount of laser energy absorbed by the flow. Figure 4(*b*) shows contours of initial temperature in a plane passing through the axis of the plasma.

A grid and time step convergence study was performed. Simulations were conducted for $T_0 = 42$ using model 2 with $\Delta x = 0.0420$, 0.0280, 0.0210 and 0.0105 and with initial $\Delta t = 10^{-3}$, 0.5×10^{-3}, 0.25×10^{-3} and 10^{-4}. The density profile perpendicular to the plasma axis at the instant when the shock wave is strongest was examined. The solution was converged for $\Delta x \leqslant 0.0210$ and $\Delta t \leqslant 0.25 \times 10^{-3}$. All reported simulations use these values of Δx and Δt.

3.1. *Results for* $T_0 = 30$

This section contains simulation results for $T_0 = 30$ obtained using model 3 described in § 2.1.3. All results are shown in non-dimensional units. The reference length scale

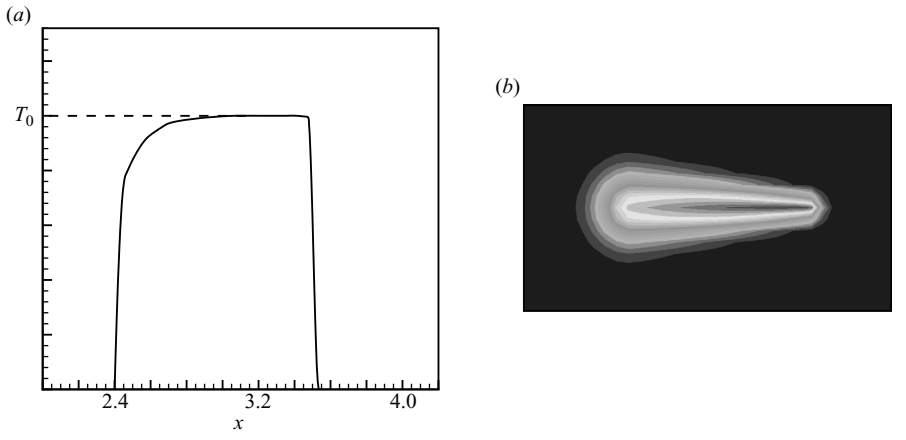

FIGURE 4. (*a*) Axial variation of the initial temperature profile. (*b*) Contours of initial temperature in a plane through the plasma axis.

L_0^* and reference time scale t_0^* (§ 2.1) are 5.55 mm and 15.99 μs, respectively, and can be used to convert the results into dimensional quantities. The dimensional plasma length used is 6.3 mm (Kandala 2005). The reference values for temperature, pressure and density are 300 K, 1 atm and 1.2 kg m^{-3}, respectively.

The flow field resulting from laser energy deposition is described in detail in this section. Energy deposition results in the formation of a blast wave that propagates into the background. Because of the initial shape of the plasma region, the blast wave is initially tear-drop shaped, but becomes spherical in time. Figure 5 shows the evolution of the temperature field obtained in the simulations. Note that the temperature field starts breaking up around $t = 0.54$. The breakup starts in the form of a dent on the right-hand side, along the axis of the plasma. This dent propagates along the plasma axis from right to left resulting in the formation of an axisymmetric temperature lobe around $t = 0.90$. In time, this temperature lobe moves further away from the plasma axis and finally rolls up to form a toroidal vortex ring as shown in the contours of temperature at $t = 1.80$. During this process, the maximum temperature is advected from the plasma axis to the centre of the vortex ring. The breaking and roll-up of the plasma core observed in this figure is a characteristic feature of the flow that has been observed in experimental flow visualization (Adelgren *et al.* 2003; Glumac *et al.* 2005*a,b*).

3.1.1. *Shock formation and propagation*

When laser energy is deposited in air, a part of it is absorbed as internal energy of the air molecules. This results in a localized energy hot spot. Since the energy deposition process is very fast, the gas density does not change significantly during this period. Hence, sharp gradients in temperature and pressure are developed within the energy spot. These gradients act as sources of acceleration on the right-hand side of the Navier–Stokes equations, and generate fluid motion. Thus the internal energy of the fluid elements is converted into kinetic energy, and a shock wave begins to form. This process continues until the shock front attains maximum intensity. Then, the shock wave propagates into the background and its strength decreases as a result.

Figure 6(*a*) shows radial profiles of density obtained normal to the axis of the plasma. Recall that the flow field is symmetric around the plasma axis. The profiles

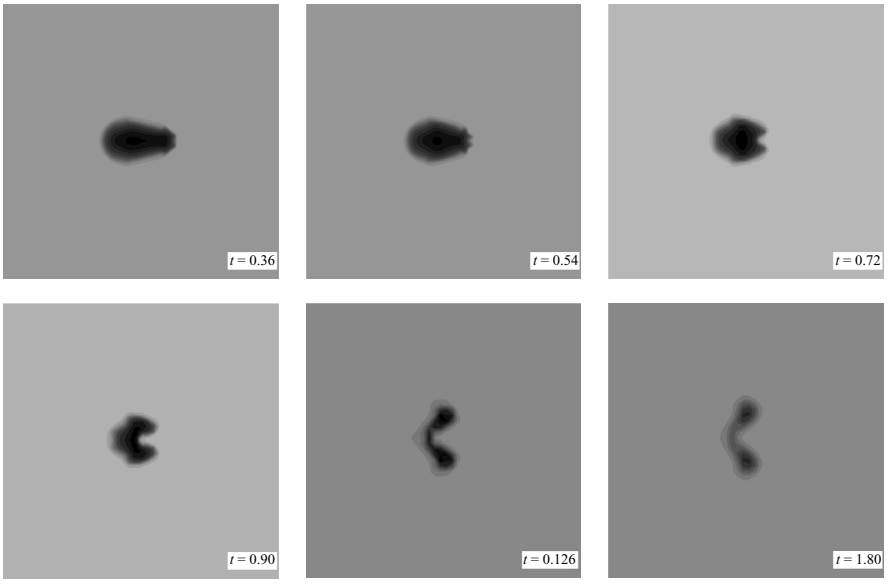

FIGURE 5. Evolution of the temperature field in time.

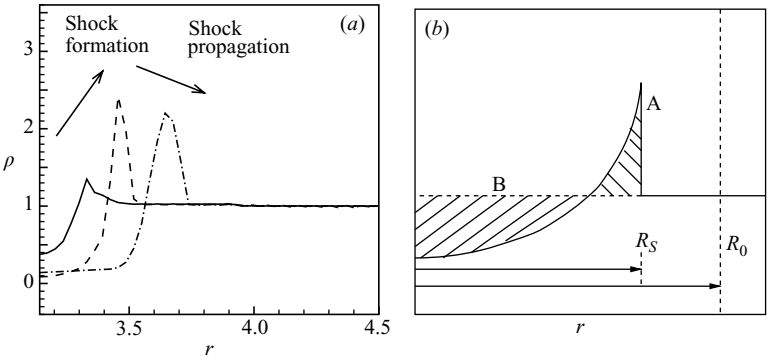

FIGURE 6. (*a*) Radial profiles of density obtained normal to the axis ($x = 3.14$) of the plasma at $t = 0.03$ (———), $t = 0.06$ (- - -) and $t = 0.15$ (—·—) showing formation and propagation of a shock wave. (*b*) Schematic representation of a shock front.

are plotted at three different instants of time. The shock-wave intensity is a maximum at $t = 0.06$. Any profile plotted before this time instant would show formation of the shock wave whereas any profile plotted after this time instant will show propagation of the shock wave into the background.

As the density at the shock front keeps increasing during shock formation, the density in the core keeps decreasing. Once shock formation is complete, the shock propagates down the domain, density at the shock front starts decreasing and the density at the core simultaneously starts increasing (figure 6). This behaviour can be explained by conservation of mass behind the shock front. Figure 6(*b*) shows a schematic of density variation behind the shock front. Consider a spherical control volume of radius R_0 around the shock wave whose radius $R_S < R_0$. The integral form

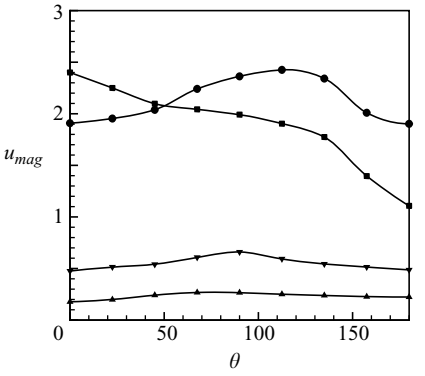

FIGURE 7. Angular variation of velocity magnitude at the shock front: ▪ , $t = 0.01$; • , $t = 0.05$; ▴ , $t = 0.36$. ▾ , $t = 0.99$.

of the continuity equation is given by

$$\int_V \left[\frac{\partial \rho}{\partial t} + \frac{\partial \rho u_j}{\partial x_j}\right] \mathrm{d}V = 0, \tag{3.1}$$

where V is the control volume under consideration. Since there is no mass flux in or out of the control volume, the second term in (3.1) becomes zero. Also assuming that the control volume is large, the shock front is confined within this volume for all time and so the control volume does not change with time. Then the time derivative in the first term of (3.1) can be taken outside the volume integral to obtain

$$\int_V \rho \, \mathrm{d}V = m_0, \tag{3.2}$$

where m_0 is a constant and is equal to the initial mass within the control volume. Thus, total mass within the control volume is conserved at all times.

At the shock front, mass accumulates owing to compression. This mass comes from the core, and hence the core experiences expansion, leading to a decrease in density. During shock formation, mass accumulation at the shock front increases and so density in the core decreases. The reverse occurs during shock propagation. At any time instant, the accumulated mass at the shock front indicated by the hatched area A has to balance the deficit of mass in the core indicated by the hatched area B.

Figure 7 shows the angular variation of maximum velocity magnitude at different instants during shock formation and propagation. Here, the angle θ is defined with respect to the plasma centre and measured away from the plasma axis from right to left. At an early stage in shock formation ($t = 0.01$), there is a sharp expansion near $\theta = 0^0$, resulting in high fluid velocities there. Strong initial temperature gradients near $\theta = 0^0$ (figure 4) yield strong pressure gradients there (figure 8*a*). Therefore, the flow undergoes a strong expansion along the x_1-direction at short times. As a result of this expansion, the pressure gradients decrease along the x_1-direction and figure 8(*b*) shows that at $t = 0.04$, strong pressure gradients are observed near $\theta = 90^0$. This behaviour is also observed in figure 7 ($t = 0.05$). The effect of the sharp gradients along the x_1-direction is momentary and the fluid velocities quickly decrease to smaller values near $\theta = 0^0$. However, the effect of the gradients perpendicular to the plasma axis is sustained, and hence generates high fluid velocities in this direction for a longer period of time.

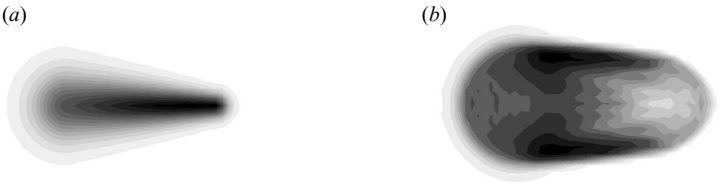

FIGURE 8. Contours of pressure at (*a*) $t = 0$ and (*b*) $t = 0.04$ showing development of a strong shock wave in the direction normal to the plasma axis.

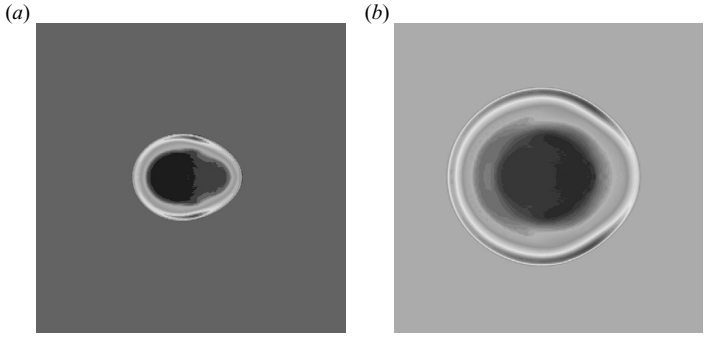

FIGURE 9. Contours of pressure at (*a*) $t = 0.36$ and (*b*) $t = 0.99$ shows that the shock wave becomes spherical in time as it propagates into the background.

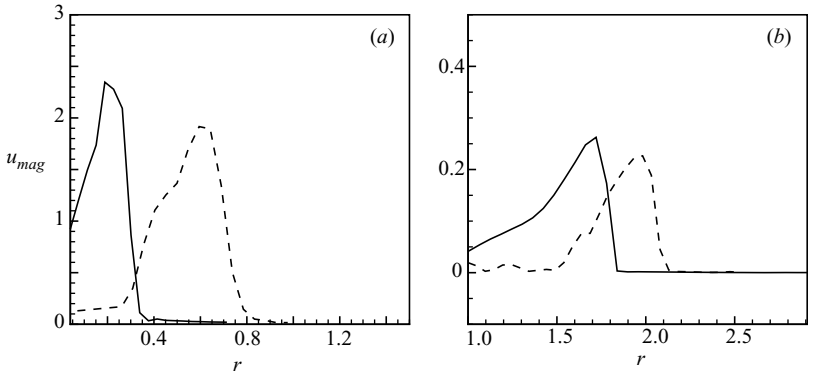

FIGURE 10. (*a*) Radial profiles for velocity magnitude plotted along different angles from the centre of the plasma at $t = 0.04$ show distinct angular asymmetry. (*b*) Similar profiles for velocity magnitude at $t = 0.99$. ——— , $\theta = 90^\circ$; – – –, $\theta = 180^\circ$.

Figure 9 shows that as the shock wave propagates into the background, it becomes spherical in shape. Also its strength becomes uniform over θ. This is also observed in the angular variation of velocity magnitude shown in figure 7. Figure 10 shows radial profiles of velocity magnitude plotted along $\theta = 90^\circ$ and $\theta = 180^\circ$ at $t = 0.05$ and 0.99. The sharper gradients perpendicular to the plasma axis at $t = 0.04$ result in stronger acceleration of the fluid elements in this direction, thus making the shock wave more spherical in time.

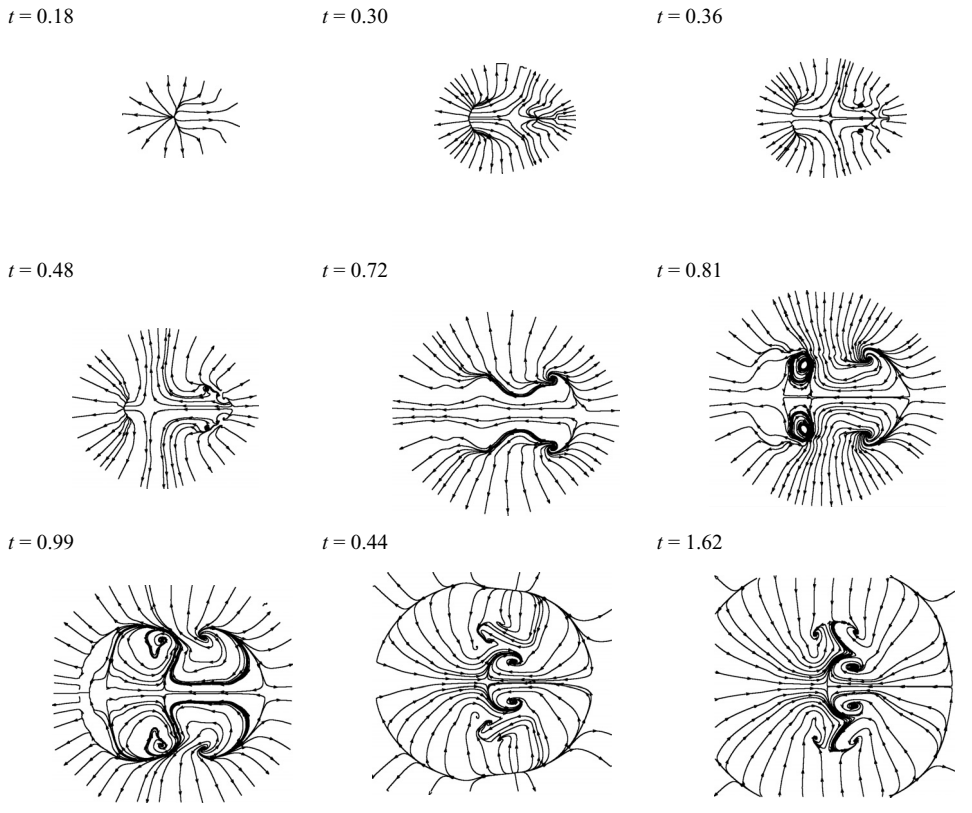

FIGURE 11. Plots of velocity streamlines showing evolution of the flow field in time.

3.1.2. *Roll-up of the plasma core*

As the shock wave propagates outwards, the temperatures in the plasma core decay in an interesting manner. The initial axial temperature profile has a single peak (figure 4*a*). In time, this peak advects to the left and yields a single centre of expansion, as observed at $t = 0.18$ in figure 11. However, the temperatures in the plasma core decay such that the axial temperature profile splits to form two independent centres of expansion ($t = 0.30$). This behaviour is also observed in experiments (e.g. Glumac *et al.* 2005*a, b*). The second expansion point is initially weaker than the first, but as the core temperatures continue to decay, the two expansion points become comparable in strength ($t = 0.36$). Since the temperatures decay faster near the first expansion point, the second expansion point soon becomes much stronger than the first. Fluid then accelerates from right to left, towards the first expansion point ($t = 0.48$). Interaction of the fluid rushing in from the right with that issuing from the first expansion point results in the flow turning normal to the plasma axis. The flow evolves to form complex vortical structures (figure 11) which finally yield the toroidal vortex ring observed in experiments (Adelgren *et al.* 2003; Glumac *et al.* 2005*a, b*).

Note that when the plasma is initially expanding, the flow along the plasma axis is from left to right. However, in time, the direction of flow along the axis is reversed. The reverse flow builds up in strength and significantly exceeds the velocity at the shock front (figure 12).

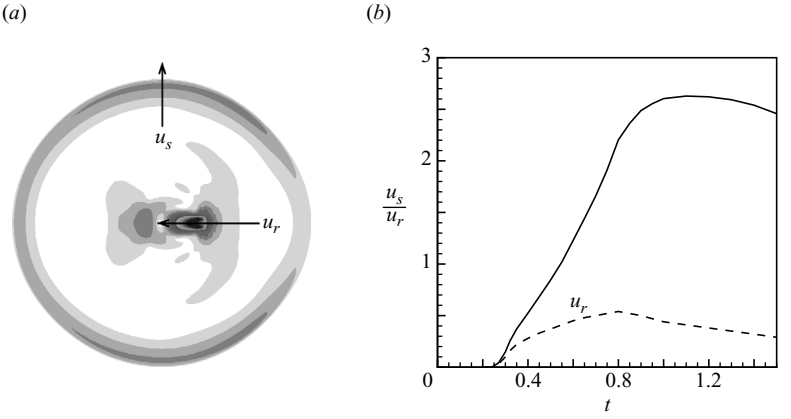

FIGURE 12. (*a*) Velocity magnitude contour showing development of a reverse flow along the plasma axis. (*b*) Plot of reverse flow velocity u_r (– – –) and the ratio of the reverse flow velocity to the maximum shock velocity u_s (———) in time.

3.1.3. *Vorticity generated in the flow*

Vorticity is generated in the flow by different processes at different times. At short times ($t < 0.30$), baroclinic production is observed to be the dominant source of vorticity in the flow. At longer times, the collapse of the plasma core described in the previous section generates vorticity. Figure 13 shows the time evolution of maximum vorticity in the flow. The first peak corresponds to baroclinic generation whereas the second peak corresponds to the reverse flow and roll-up of the plasma core. Figure 14(*a*) shows contours of vorticity magnitude at $t = 0.24$ in a plane passing through the plasma axis. The vorticity is negative and positive near the leading and trailing edges of the plasma core, respectively. Here, leading edge refers to the edge closer to the laser source. Also, the vorticity is stronger near the trailing edge.

The vorticity equation for a compressible viscous flow with variable fluid properties is

$$\frac{\partial \boldsymbol{\omega}}{\partial t} = \underbrace{-(\boldsymbol{u}\cdot\nabla)\boldsymbol{\omega}}_{\text{convection}} + \underbrace{(\boldsymbol{\omega}\cdot\nabla)\boldsymbol{u}}_{\text{vortex stretching/tilting}} - \underbrace{\boldsymbol{\omega}(\nabla\cdot\boldsymbol{u})}_{\text{bulk dilatation}} \underbrace{-\frac{\nabla p\times\nabla\rho}{\rho^2}}_{\text{baroclinic}} + \frac{1}{Re}\underbrace{\left(\nabla\times\left(\frac{1}{\rho}\nabla\cdot\tau\right)\right)}_{\text{viscous}}. \tag{3.3}$$

Budgets are computed for the different terms on the right-hand side of (3.3) and their behaviour in time is observed at two representative points near the leading ($x = 2.7$, $y = 3.48$) and trailing ($x = 3.45$, $y = 3.33$) edges of the plasma (figure 14*b*,*c*). The baroclinic term is the dominant contributor to vorticity production. The baroclinic term is negative and positive near the leading and trailing edges, respectively, consistent with the sign of vorticity. Also, the baroclinic term is stronger near the trailing edge. This is because the densities are lower there, and also because the shock curvature changes more rapidly near the trailing edge, resulting in larger misalignment between the density and the pressure gradients.

The bulk dilatation term is negative and positive near the leading and trailing edges of the plasma, respectively. Since the flow is expanding behind the shock wave, $\nabla\cdot\boldsymbol{u}$ is positive there. Since ω is positive and negative near the leading and

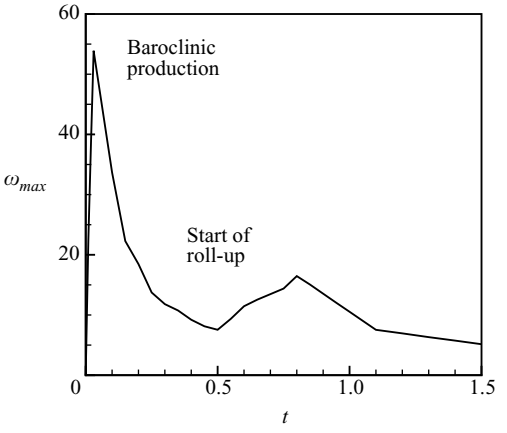

FIGURE 13. Evolution of maximum vorticity magnitude in time.

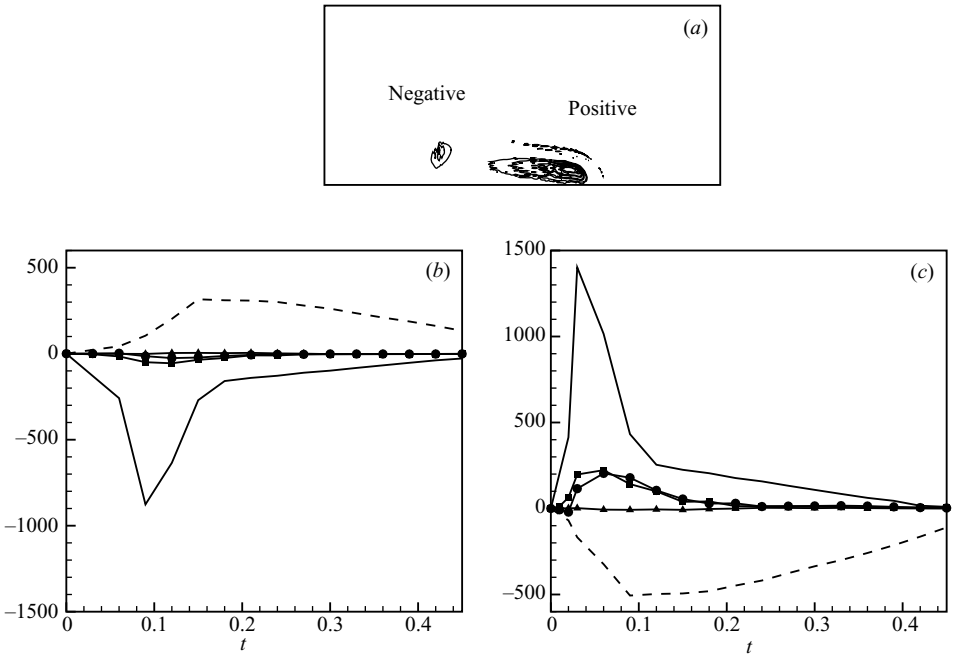

FIGURE 14. (*a*) Vorticity contours shown at $t = 0.24$. (*b*) Budgets for different terms in the vorticity transport equation computed near the leading edge of the plasma. (*c*) Budgets for the vorticity transport equation computed near the trailing edge. ——— , baroclinic term; – – –, bulk dilatation term; ▪ , convection term; ● , vortex stretching/tilting term; ▲ , viscous term.

trailing edges, respectively, the bulk dilatation terms are correspondingly negative and positive in these regions. Also, the magnitude of the bulk dilatation term peaks much later in time compared to the baroclinic term. The convection and the vortex stretching/tilting terms have the same sign as the baroclinic term, but are much smaller in magnitude. The viscous term is observed to be the smallest, since *Re* for the flow is very high. Combining the effects of the different terms, it can be concluded that as the blast wave propagates, it leaves behind misaligned density and pressure

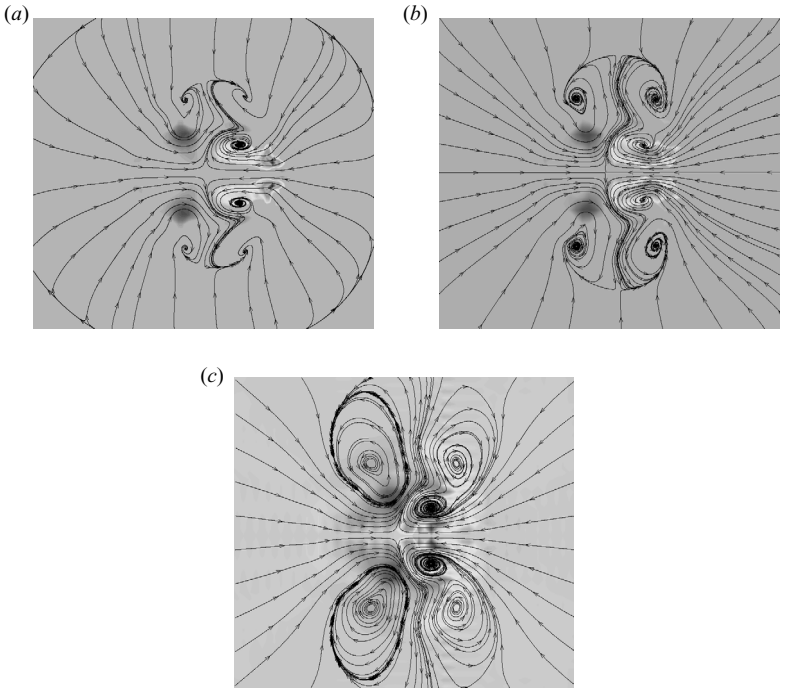

FIGURE 15. Velocity streamlines plotted over contours of vorticity magnitude at (*a*) $t = 1.60$, (*b*) $t = 2.0$ and (*c*) $t = 2.40$.

gradients. These gradients generate baroclinic vorticity, which is eventually suppressed by the expansion behind the shock wave.

At long times, vorticity is generated because of the collapse of the plasma core (described in § 3.1.2). The actual vorticity field is much more complicated than merely a single toroidal vortex ring as observed in experiments of laser-induced breakdown (Adelgren *et al.* 2001). However, the magnitude of vorticity is much stronger in the vortex ring closest to the plasma axis (figure 15). Hence, only a single toroidal vortex ring is observed in the experimental flow visualization.

3.2. *Parametric study*

Recall that the relevant parameters associated with the problem are the shape and size of the initial plasma region, the maximum temperature ratio in the plasma core T_0 and Reynolds number of the flow. The effects of change in T_0 and the Reynolds number on the resulting flow field are discussed in the following sections. All simulations in this section use model 3 described in § 2.1.3.

3.2.1. *Effect of* T_0

The shape and size of the initial plasma region is the same as that used in the previous simulations and is assumed to be independent of T_0 over the range for which the simulations are performed. Results are shown for $T_0 = 30$, 36 and 42. Viscosity for air is computed assuming equilibrium as discussed in § 2.1.

The higher the value of T_0, the stronger the initial gradients in the pressure field. Hence, a stronger shock wave develops with increase in T_0. Figure 16(*a*) shows radial profiles of pressure computed normal to the plasma axis at the end of shock formation. Note that the maximum intensity for the developed shock wave is highest

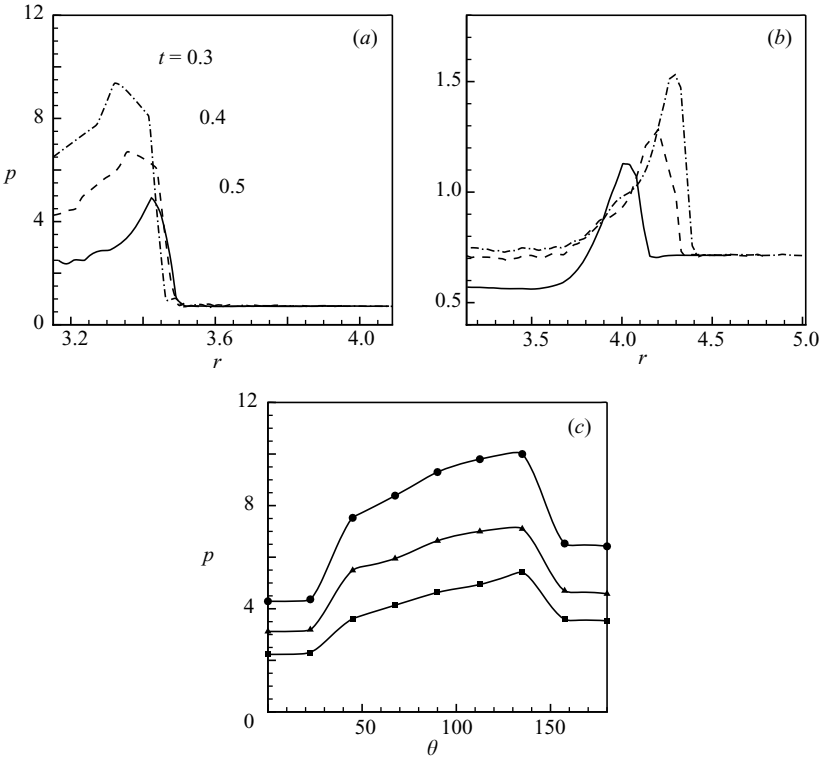

FIGURE 16. (*a*) Radial pressure profiles ($\theta = 90°$) for $T_0 = 30$ (———), $T_0 = 36$ (– – –) and $T_0 = 42$ (—·—) at the end of shock formation for each case. (*b*) Radial pressure profiles ($\theta = 90°$) for $T_0 = 30$ (———), $T_0 = 36$ (– – –) and $T_0 = 42$ (—·—) at $t = 0.45$. (*c*) Angular variation of pressure at the shock front at the instant when it is maximum. ■ , $T_0 = 30$; ▲ , $T_0 = 36$; ● , $T_0 = 42$.

for $T_0 = 42$. Also, the shock formation time is smallest for $T_0 = 42$ and largest for $T_0 = 30$. The process of conversion of internal energy into kinetic energy is also faster with increase in energy deposited.

Since the pressure gradients are strongest for $T_0 = 42$, higher shock velocities are developed. Thus, if profiles are compared at the same time instant, the shock wave for $T_0 = 42$ will have propagated farthest (figure 16*b*). Profiles of pressure computed normal to the plasma axis at $t = 0.45$ are shown for different T_0. The shock radius is largest for $T_0 = 42$ and smallest for $T_0 = 30$. Figure 16(*c*) shows the angular variation of pressure at the shock front at the end of the shock-formation process. The angle θ is defined as described in § 3.1.1. Note that the shock strength increases with increase in T_0, but the angular spread of the shock strength does not change much.

Figure 17(*a*) shows the maximum reverse flow magnitude u_r for different T_0. For higher T_0, stronger reverse flows are obtained. However, the overall trend remains the same for different T_0. Recall that this reverse flow was found to be responsible for generating vorticity in the flow at long times. Figure 17(*b*) shows evolution of the maximum vorticity magnitude in time for different T_0. The stronger the reverse flow developed, the higher the magnitude of vorticity generated. Also the baroclinic vorticity generated at short times is observed to be stronger for higher T_0. This is because, as discussed in § 3.1.3, the baroclinic vorticity generated depends directly

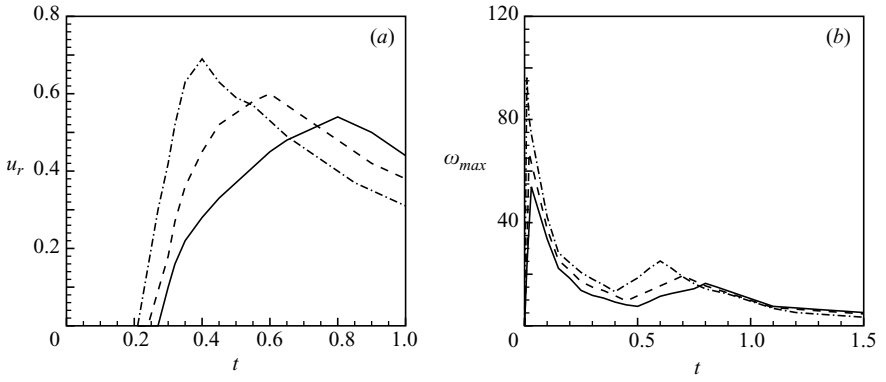

FIGURE 17. (*a*) Time evolution of the maximum reverse flow magnitude for different T_0. (*b*) Time evolution of the maximum vorticity magnitude for different T_0. ——— , $T_0 = 30$; – – –, $T_0 = 36$; —·— , $T_0 = 42$.

T_0	Maximum initial pressure	Maximum velocity at shock front	Maximum baroclinic vorticity	Maximum vorticity due to roll-up	Shock formation time	Roll-up begin time
30.0	35.23	2.40	53.90	16.46	0.05	0.27
36.0	49.65	2.73	67.20	19.41	0.04	0.24
42.0	61.67	3.35	96.20	25.12	0.03	0.21

TABLE 1. Effect of T_0 on different flow quantities.

on the local shock strength which increases with increase in T_0. Also, the process of setting up the reverse flow and the generation of vorticity in the flow speeds up with increase in T_0.

Table 1 provides a quantitative description of how the flow varies with T_0. All quantities are non-dimensional as discussed in § 2.1. Also, the shock formation time is obtained based on maximum pressure gradients at the shock front. The time at which roll-up begins is defined as the instant when $u/u_s = 0.01$.

3.2.2. *Effect of Reynolds number*

The Reynolds number Re is defined in § 2.1 and is obtained as 1.27×10^5. Re is computed using the values for the length of the plasma region, density of air and reference temperature stated in § 3.1 and viscosity of air $\mu = 1.73 \times 10^{-5}\,\mathrm{ns\,m^{-2}}$. The effect of Re on the flow is discussed in this section.

Figure 18(*a*) shows temperature contours at $t = 1.8$ and $Re = 1200$. Comparison to the time evolution of the temperature field shown in figure 5 shows that the core of the plasma does not roll up for low Re. Figure 18(*b*) shows velocity streamlines obtained at the same time instant. Fluid elements move in along the plasma axis from both directions, and do not turn normal to the plasma axis. Comparison to the velocity streamlines shown in figure 11 indicates that the sequential evolution of the velocity field that eventually results in rolling up of the plasma core does not occur for the low Re case. These results can be attributed to enhanced viscous dissipation resulting from the decrease in Re. The effect of numerical dissipation will be similar, and so it is important to minimize numerical dissipation in such simulations.

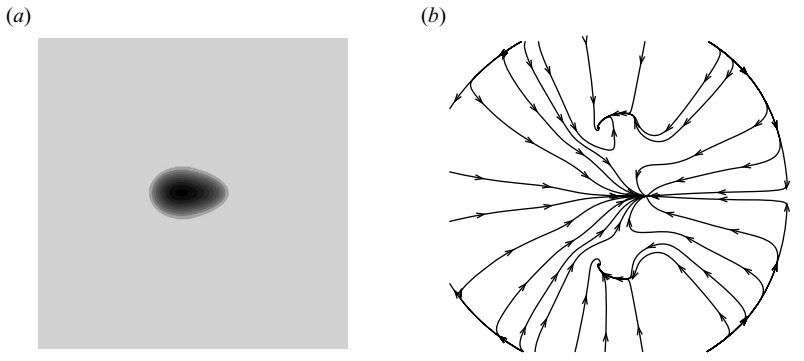

FIGURE 18. (*a*) Temperature contours and (*b*) velocity streamlines at $t = 1.80$ show that for $Re = 1200$ the core of the plasma does not roll up in time.

3.3. *Comparison between different models*

Various simulation models have been used in the past to model different aspects of laser-induced breakdown in air. Some complicated models have not been able to predict correctly the experimentally observed time evolution of the resulting flow field. However, other simpler models can easily predict the breaking and roll-up of the plasma core. The objective of this section is to investigate the minimum level of physical complexity that would be required for a model to predict breaking and roll-up of the core. This section also discusses how adding different physical aspects to the model influence the initial conditions and the time evolution of the resulting flow field. Results obtained from three different simulation models are compared. Recall that for the first model, the effects of chemical reactions are neglected. In other words, all the properties for air have been assumed to be constant. For the second model, the effect of temperature variation on the thermodynamic and transport properties of air are considered. For the third model, the effect of both temperature and pressure variation on the properties of air are accounted for. The details of the simulation methodology used for the different models have been discussed in § 2.

All simulations in this section are conducted for $T_0 = 30$. Figure 19 shows the initial pressure profiles obtained for the three different models. Note that the maximum initial pressure obtained is significantly different for the three models. For all three models, the initial pressure profile is obtained from the relation

$$p^* = \rho^* R^* T^*, \tag{3.4}$$

used in a suitable non-dimensional form. For the first model, $R^* = R_0^*$ and is a constant. So the pressures obtained are low. For the second model, owing to the effect of chemical reactions, the value of R^* at higher temperatures is significantly greater than ${R_0}^*$ (figure 3*c*). Thus, the initial pressures are much higher in this case. For the third model, with increase in pressure, the value of R^* decreases at higher temperatures (figure 3*c*). The initial pressures therefore are intermediate to the other two models.

Table 2 shows how different flow variables vary with the model used. All quantities are in non-dimensional form (§ 2.1). The angular variation of maximum pressure at the shock front shows (figure 20*a*) that even though the angular profiles are very similar for the different models, the pressure levels are quite different. Highest pressures are obtained for model 2 and lowest are obtained for model 1. Radial pressure profiles computed normal to the plasma axis at $t = 0.45$ (figure 20*b*) confirm this observation.

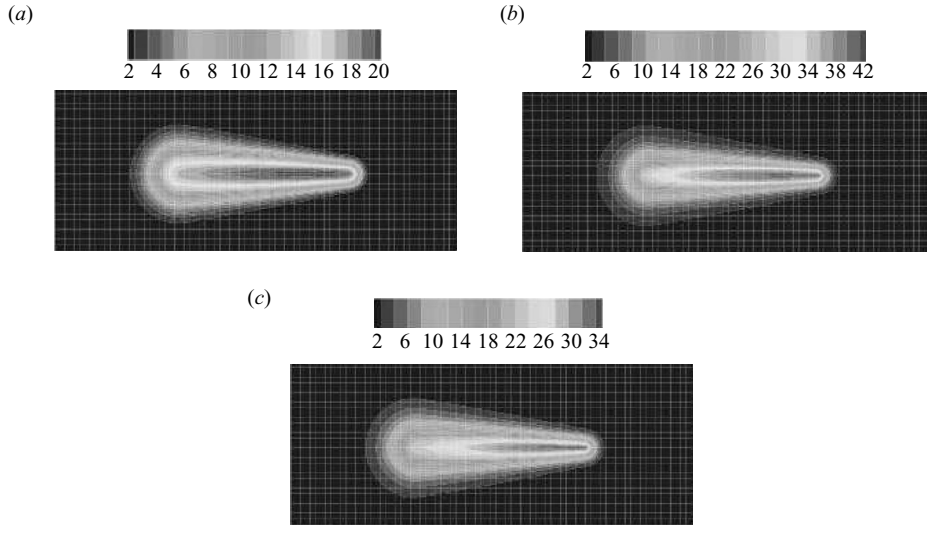

FIGURE 19. Initial pressure contours obtained for three different models, (*a*) model 1, (*b*) model 2 and (*c*) model 3.

Model ($T_0 = 30$)	Maximum initial pressure	Maximum velocity at shock front	Maximum baroclinic vorticity	Maximum vorticity due to roll-up	Shock formation time	Roll-up begin time
1	21.07	1.69	28.45	12.06	0.06	0.30
2	42.89	2.87	63.78	18.81	0.04	0.25
3	35.23	2.40	53.90	16.46	0.05	0.27

TABLE 2. Variation of different flow quantities with the simulation model used.

The evolution of the flow field is qualitatively similar for all three models (figure 21). However, the extent to which the flow has evolved at any given time is different. At any instant, all three models yield different stages of the characteristic flow evolution sequence shown in figure 11. Since the pressure gradients are weakest for the first model, the flow field evolves slowly when compared to the other cases. Hence, only a single expansion centre is observed. For the second model, the flow field evolves faster than the other cases. Hence, two distinct expansion centres of comparable strength are observed. The flow field obtained from model 3 evolves to a stage intermediate between that obtained from models 1 and 2. For all three models, the flow field eventually rolls up. Even an ideal-gas representation is sufficient to predict the roll-up of the plasma core.

4. Summary

This paper uses numerical simulation to study the effect of laser energy deposition on quiescent air. Local thermodynamic equilibrium conditions are assumed to apply. The simulations solve the compressible Navier–Stokes equations using Fourier spectral methods. A predictor–corrector-based shock-capturing scheme is incorporated to account for the strong shock waves. Three different models are used to obtain the thermodynamic and transport properties for air. For model 1, the effects of the

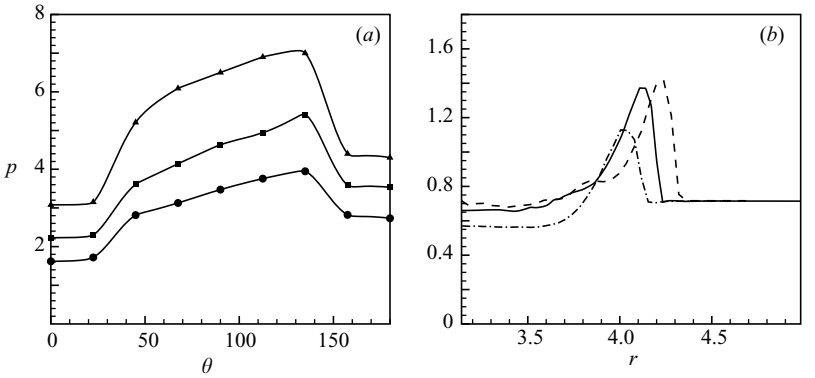

FIGURE 20. (*a*) Angular variation of pressure at the shock front at the instant when it is maximum. •, model 1; ▲, model 2; ■, model 3. (*b*) Radial pressure profiles ($\theta = 90^0$) for model 1 (—·—), model 2 (– – –) and model 3 (———) at $t = 0.45$.

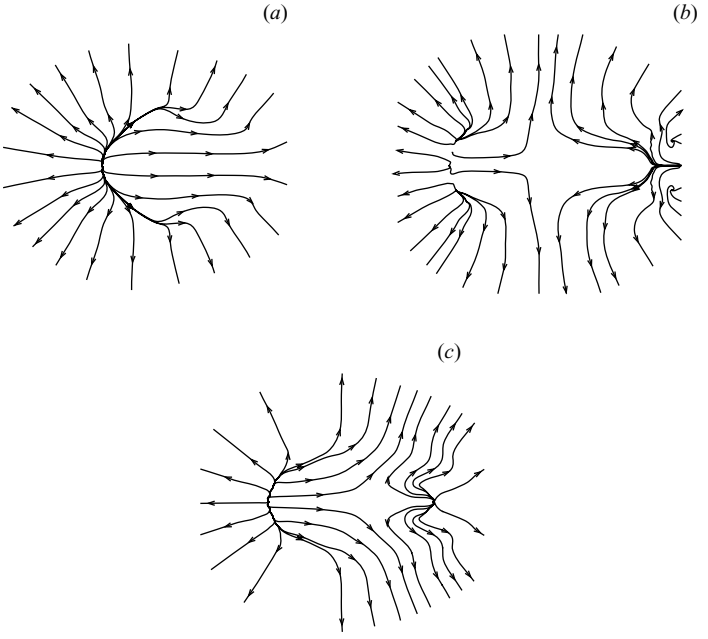

FIGURE 21. Comparison of velocity streamlines from different models at $t = 0.3$, (*a*) model 1, (*b*) model 2 and (*c*) model 3.

chemical reactions are neglected and fluid properties are assumed to be constant. For model 2, the properties are assumed to vary with temperature alone. Model 3 accounts for both temperature and pressure variation of the properties of air. For each model, the corrector step of the shock-capturing scheme is suitably modified. Also, a logarithmic formulation for the continuity equation is developed to handle low densities at the core of the plasma.

The evolution of the flow field is classified into formation of a shock wave, its propagation into the background and subsequent collapse of the plasma core. Each phase is studied in detail. Formation and propagation of the shock wave is explained based on conservation of mass behind the shock front. The flow is driven by the

gradients in the pressure field. The shock wave is stronger normal to the plasma axis and the angular variation of the shock strength is discussed. As the shock wave propagates into the background, its asymmetry decreases and it becomes spherical in time.

Behind the shock wave, a strong reverse flow is observed along the plasma axis. This reverse flow initially increases in strength to a maximum and then gradually decays. The reverse flow generates a complicated vortical field with a prominent toroidal ring vortex. The process is explained.

Vorticity is generated in the flow through different mechanisms. At short times, vorticity is generated by baroclinic means. At longer times, vorticity is generated as a result of the reverse flow in the plasma core.

The effects of deposited laser energy and Reynolds number are discussed. Jumps at the shock front scale with the initial pressure gradients and hence with the amount of energy deposited in the flow. However, the propagation of the shock wave and formation of the reverse flow are qualitatively similar for different amount of energy deposited. The plasma core does not roll-up at very low Re.

Results obtained from simulations conducted using three different models for air are compared. The initial pressure fields are found to be significantly different for the three models. Again, the results are found to scale with the initial gradients in the pressure field. However, the flow field is found to evolve in a qualitatively similar manner for all three models.

This work is supported by the United States Air Force Office of Scientific Research under grant FA-9550-04-1-0064. Computing resources were provided by the Minnesota Supercomputing Institute, the San Diego Supercomputing Center, and the National Center for Supercomputing Applications. We are thankful to Dr Noma Park for useful discussions.

Appendix

The Jacobian matrix for the corrector step of the shock-capturing scheme is reconstructed based on the assumption that the thermodynamic properties are functions of pressure and temperature. The Jacobian matrix for the x-direction is obtained as

$$\boldsymbol{J}_x = \begin{pmatrix} 0 & 1 & 0 & 0 & 0 \\ \left(-u^2 + \dfrac{1}{\theta_1}(RT - G_1 - A(e - e_k))\right) & \left(2 - \dfrac{A}{\theta_1}\right)u & -\dfrac{A}{\theta_1}v & -\dfrac{A}{\theta_1}w & \dfrac{A}{\theta_1} \\ -vu & v & u & 0 & 0 \\ -wu & w & 0 & u & 0 \\ -(A'(e - e_k) + e_0 + G_1 + G_1G_2 - RTG_2) & (e_0 + RT - A'u^2) & -A'uv) & -A'uw) & (1 + A')u \end{pmatrix}$$

where A' and A are given by,

$$A' = A(1 + G_2), \quad A = \left(R + T\frac{\partial R}{\partial T}\right)\frac{1}{\theta_2}, \tag{A1}$$

G_1 and G_2 are given by

$$G_1 = \frac{Ap}{\theta_1}\frac{\partial e}{\partial p}, \quad G_2 = \frac{\rho T}{\theta_1}\frac{\partial R}{\partial p}, \tag{A2}$$

and θ_1 and θ_2 are given by

$$\theta_1 = \left(1 - \frac{p}{R}\frac{\partial R}{\partial p}\right), \quad \theta_2 = \frac{\partial e}{\partial T} + \frac{\partial e}{\partial p}\left(\frac{\dfrac{p}{T} + \dfrac{p}{R}\dfrac{\partial R}{\partial T}}{1 - \dfrac{p}{R}\dfrac{\partial R}{\partial p}}\right). \tag{A3}$$

This form of the Jacobian matrix is used for simulations using model 3. The right and left eigen vector matrices R and L are computed numerically. Note that the Jacobian matrix is easily reducible to models 2 and 1. For model 2, the gradients of e and R with respect to pressure are neglected. Hence, G_1 and G_2 become

$$G_1 = G_2 = 0, \tag{A4}$$

θ_1 and θ_2 simplify to give

$$\theta_1 = 1, \quad \theta_2 = \frac{\mathrm{d}e}{\mathrm{d}T}, \tag{A5}$$

and

$$A' = A = \left(R + T\frac{\partial R}{\partial T}\right)\frac{\mathrm{d}T}{\mathrm{d}e}. \tag{A6}$$

The Jacobian matrix is given by

$$\boldsymbol{J}_x = \begin{pmatrix} 0 & 1 & 0 & 0 & 0 \\ (-u^2 + RT - A(e - e_k)) & (2 - A) * u & -Av & -Aw & A \\ -vu & v & u & 0 & 0 \\ -wu & w & 0 & u & 0 \\ -(e_0 + A(e - e_k))u & (e_0 + RT - Au^2) & -Auv & -Auw & (1 + A)u. \end{pmatrix}.$$

Define a set of variables e_1 and e_2 such that

$$e_1 = \frac{{c_1}^2}{A(A + 1)} \tag{A7}$$

and

$$e_2 = e - e_1. \tag{A8}$$

Also define ${e_k}^*$ such that

$${e_k}^* = e_k - e_2. \tag{A9}$$

Then the right and left eigen vector matrices R and L for the x-direction are then obtained as

$$\boldsymbol{R}_x = \begin{pmatrix} 1 & 1 & 1 & 0 & 0 \\ u - c_1 & u & u + c_1 & 0 & 0 \\ v & v & v & -1 & 0 \\ w & w & w & 0 & 1 \\ (h_0 - c_1 u) & {e_k}^* & (h_0 + c_1 u) & -v & w \end{pmatrix},$$

and

$$\boldsymbol{R}_X = \begin{pmatrix} \dfrac{Ae_k^* + c_1 u}{2{c_1}^2} & -\dfrac{Au + c_1}{2{c_1}^2} & -\dfrac{Av}{2{c_1}^2} & -\dfrac{Aw}{2{c_1}^2} & \dfrac{A}{2{c_1}^2} \\ \dfrac{{c_1}^2 - Ae_k^*}{{c_1}^2} & \dfrac{Au}{{c_1}^2} & \dfrac{Av}{{c_1}^2} & \dfrac{Aw}{{c_1}^2} & -\dfrac{A}{{c_1}^2} \\ \dfrac{Ae_k^* - c_1 u}{2{c_1}^2} & -\dfrac{Au - c_1}{2{c_1}^2} & -\dfrac{Av}{2{c_1}^2} & -\dfrac{Aw}{2{c_1}^2} & \dfrac{A}{2{c_1}^2} \\ v & 0 & -1 & 0 & 0 \\ -w & 0 & 0 & 1 & 0 \end{pmatrix}$$

where h_0 is the total enthalpy given by

$$h_0 = h + e_k. \tag{A10}$$

Similarly, eigen vectors R_Y, R_Z, L_Y and L_Z can be computed along the y- and z-directions, respectively.

The Jacobian matrix can be further be simplified for model 1. Then A further simplifies to

$$A = (\gamma - 1), \tag{A11}$$

and the Jacobian matrix is given by

$$\boldsymbol{J}_x = \begin{pmatrix} 0 \\ (-u^2 + RT - (\gamma - 1)(e - e_k)) \\ -vu \\ -wu \\ -(e_0 + (\gamma - 1)(e - e_k))u \end{pmatrix}$$

$$\begin{pmatrix} 1 & 0 & 0 & 0 \\ (3 - \gamma) * u & -(\gamma - 1)v & -(\gamma - 1)w & (\gamma - 1) \\ v & u & 0 & 0 \\ w & 0 & u & 0 \\ (e_0 + RT - (\gamma - 1)u^2) & -(\gamma - 1)uv & -(\gamma - 1)uw & \gamma u \end{pmatrix}.$$

Thus, the Jacobian matrix then reduces to its standard low-temperature form (Rohde 2001). Similar Jacobian matrices can be constructed for the y- and z-directions. The eigen vector matrices R and L can be similarly simplified.

REFERENCES

Adelgren, R., Boguszko, M. & Elliott, G. 2001 Experimental summary report – shock propagation measurements for Nd:YAG laser induced breakdown in quiescent air. Department of Mechanical and Aerospace Engineering, Rutgers University.

Adelgren, R. G., Yan, H., Elliott, G. S., Knight, D., Beutner, T. J., Zheltovodov, A., Ivanov, M. & Khotyanovsky, D. 2003 Localized flow control by laser energy deposition applied to Edney IV shock impingement and intersecting shocks. *AIAA Paper* 2003–31.

Blaisdell, G. A., Mansour, N. N. & Reynolds, W. C. 1991 Numerical simulations of compressible homogeneous turbulence. Report TF-50, Thermosciences Division, Department of Mechanical Engineering, Stanford University.

Brode, H. L. 1955 Numerical solution of blast waves. *J. Appl. Phys.* **26**, 766–775.

Damon, E. & Tomlinson, R. 1963 Observation of ionization of gases by a ruby laser. *Appl. Optics* **2**, 546–547.

Dors, I. G. & Parigger, C. G. 2003 Computational fluid-dynamic model of laser induced breakdown in air. *Appl. Optics* **42**, 5978–5985.

Dors, I., Parigger, C. & Lewis, J. 2000 Fluid dynamic effects following laser-induced optical breakdown. *AIAA Paper* 2000–0717.

Glumac, N., Elliott, G. & Boguszko, M. 2005*a* Temporal and spatial evolution of thermal structure of laser spark in air. *AIAA J.* **43**, 1984–1994.

Glumac, N., Elliott, G. & Boguszko, M. 2005*b* Temporal and spatial evolution of the thermal structure of a laser spark in air. *AIAA Paper* 2005–0204.

Harten, A. 1978 The artificial compression method for computation of shocks and contact discontinuities. *Maths Comput.* **32**, 363.

Hayes, W. D. 1957 The vorticity jump across a gasdynamic discontinuity. *J. Fluid Mech.* **2**, 595–600.

Jiang, Z., Takayama, K., Moosad, K. P. B., Onodera, O. & Sun, M. 1998 Numerical and experimental study of a micro-blast wave generated by pulsed laser beam focusing. *Shock waves* **8**, 337–349.

Kandala, R. 2005 Numerical simulations of laser energy deposition for supersonic flow control. PhD thesis, Department of Aerospace Engineering and Mechanics, University of Minnesota.

Kandala, R. & Candler, G. 2003 Numerical studies of laser-induced energy deposition for supersonic flow control. *AIAA Paper* 2003–1052.

Kandala, R., Candler, G., Glumac, N. & Elliott, G. 2005 Simulation of laser-induced plasma experiments for supersonic flow control. *AIAA Paper* 2005–0205.

Keefer, D. 1989 Laser-sustained plasmas. In *Laser-Induced Plasmas and Applications* (ed. L. J. Radziemski & D. A. Cremers) Marcel Dekker.

Knight, D., Kuchinskiy, V., Kuranov, A. & Sheikin, E. 2003 Survey of aerodynamic flow control at high speed by energy deposition. *AIAA Paper* 2003–0525.

Lee, J. H. 2005 Electron-impact vibrational relaxation in high temperature nitrogen. *AIAA Paper* 1992–0807.

Lewis, J., Parigger, C., Hornkohl, J. & Guan, G. 1999 Laser-induced optical breakdown plasma spectra and analysis by use of the program NEQAIR. *AIAA Paper* 99–0723.

McBride, B. J. & Gordon, S. 1961 Thermodynamic functions of several triatomic molecules in the ideal gas state. *J. Chem. Phys* **35**, 2198–2206.

McBride, B. J. & Gordon, S. 1967 FORTRAN IV program for calculation of thermodynamic data. *NASA SP* 3001.

McBride, B. J. & Gordon, S. 1976 Computer program for computation of complex chemical equilibrium compositions, rocket performance, incident and reflected shocks, and Chapman–Jouguet detonations. *NASA SP* 273.

McBride, B. J. & Gordon, S. 1992 Computer program for calculating and fitting thermodynamic functions. *NASA RP* 1271.

McBride, B. J., Heimel, S., Ehlers, J. & Gordon, S. 1963 Thermodynamic properties to 6000 K for 210 substances involving the first 18 elements. *NASA SP* 3001.

Maker, P., Terhune, R. & Savage, C. 1963 *Proc. Third Intl. Quantum Mechanics Conf. Paris.*

Meyerand, R. & Haught, A. 1963 Gas breakdown at optical frequencies. *Phys. Rev. Lett.* **11**, 401–403.

Molina-Morales, P., Toyoda, K., Komurasaki, K. & Arakawa, Y. 2001 CFD simulation of a 2-kW class laser thruster. *AIAA Paper* 2001–0650.

Morgan, C. 1975 Laser-induced breakdown of gases. *Rep. Prog. Phys.* **38**, 621–665.

Phuoc, T. X. 2000 Laser spark ignition: experimental determination of laser-induced breakdown thresholds of combustion gases. *Optics Commun.* **175**, 419–423.

Phuoc, T. X. 2005 An experimental and numerical study of laser-induced spark in air. *Optics Lasers Engng* **43**, 113–129.

Raizer, Y. P 1966 Breakdown and heating of gases under the influence of a laser beam. *Sov. Phys. USPEKHI* **8**, 650–673.

Riggins, D. W., Nelson, H. F. & Johnson, E. 1999 Blunt-body wave drag reduction using focused energy deposition. *AIAA J.* **37**, 460–467.

Rohde, A. 2001 Eigen values and eigen vectors of the Euler equations in general geometries. *AIAA Paper* 2001–2609.

Root, R. G. 1989 *Modeling of Post-Breakdown Phenomenon in Laser-Induced Plasma and Applications*, vol. 2, pp. 69–103. Marcel Dekker.

Shneider, M. N., Macheret, S. O., Zaidi, S. H., Girgis, I. G., Raizer, Yu. P. & Miles, R. B. 2003 Steady and unsteady supersonic flow control with energy addition. *AIAA Paper* 2003–3862.

Steiner, H., Gretler, W. & Hirschler, T. 1998 Numerical solution for spherical laser-driven shock waves. *Shock Waves* **8**, 337–349.

Wang, T. S., Chen, Y. S., Liu, J., Myrabo, L. N. & Mead, F. B. 2001 Advanced performance modeling of experimental laser lightcrafts. *AIAA Paper* 2001–0648.

Yan, H., Adelgren, M., Bouszko, M., Elliott, G. & Knight, D. 2003 Laser energy deposition in quiescent air *AIAA Paper* 2003–1051.

Yee, H. C., Sandham, N. D. & Djomehri, M. J. 1999 Low-dissipative high-order shock-capturing methods using characteristic-based filter. *J. Comput. Phys.* **150**, 199–238.